Asian Journal of Chemistry; Vol. 38, No. 11 (2026), 2883-2890
ASIAN JOURNAL OF CHEMISTRY
https://doi.org/10.14233/ajchem.2026.36705

Layered Mesoporous Marigold Like PANI-MnO_2 Nanocomposites *via* Static Interfacial Polymerization for Enhanced Electrochemical Energy Storage

SANGITA SATPUTE[1,2,*], MILIND KULKARNI[2] and GAURAV THORAT[3]

[1]Department of Chemistry, Vidya Pratishthan's ASC College, Baramati-413133, India
[2]Nanocomposite Laboratory, Centre for Materials for Electronics Technology, Department of Electronics and Information Technology (Government of India), Panchawati, Off Pashan Road, Pune-411008, India
[3]InoBat, Bratislava, Slovakia

*Corresponding author: E-mail: sangitathoratvp@gmail.com

Received: 24 June 2026 *Accepted*: 17 September 2026 *Published online*: 13 November 2026 AJC-22518

A mesoporous marigold-like PANI-MnO_2 nanocomposite with a layered hollow architecture was synthesized *via* a static interfacial polymerization method, wherein $KMnO_4$ served simultaneously as the oxidant and MnO_2 as precursor. The synthesized PANI-MnO_2 nanocomposite exhibited a hierarchical, marigold-like architecture comprising interconnected mesopores and hollow macroporous domains. Its structural and physico-chemical characteristics were investigated using UV–Vis and FT-IR spectroscopy, X-ray diffraction (XRD), thermogravimetric and differential thermal analysis (TG-DTA) and electron microscopy. The hierarchical porous structure is expected to facilitate electrolyte transport, while the hollow macroporous domains may serve as ion-buffering reservoirs, promoting ion accessibility and reversible redox reactions during charge–discharge cycling. Electrochemical testing in a three-electrode cell using 1 M KOH as the electrolyte yielded a quasi-rectangular cyclic voltammogram with distinct redox peaks, which is consistent with capacitive charge storage accompanied by Faradaic reactions. The PANI-MnO_2 nanocomposite delivered a specific capacitance of 223 F g^{-1} at a current density of 10 A g^{-1} and retained approximately 91% of its initial capacitance after 2500 charge–discharge cycles. The combination of specific capacitance and cycling retention points to the potential of the marigold-like porous architecture for electrode applications in electrochemical energy storage.

Keywords: Polyaniline, MnO_2 nanocomposite, Interfacial polymerization, Mesoporous nanofibers, Supercapacitor.

INTRODUCTION

Transition metal oxides, intrinsically conducting polymers and carbon-based materials are widely investigated as electroactive materials for batteries and electrochemical supercapacitors [1-3]. Conducting polymers have received considerable attention for their reversible doping–dedoping behaviour, electrical conductivity, processability and electrochemical activity [3,4]. Their practical use, though, remains constrained by limited mechanical stability, volume changes during charge–discharge cycling and a gradual loss of conductivity during repeated doping–dedoping processes [5]. Combining conducting polymers with transition metal oxides or carbonaceous materials offers a means of addressing these limitations while improving charge-storage characteristics [1,3,5-7]. Transition metal oxides such as RuO_2, SnO_2, NiO, MnO_2 and V_2O_5 can store charge through reversible redox reactions involving different oxidation states [2,6]. Among these materials, MnO_2 is attractive for electrochemical applications, although its low intrinsic electrical conductivity and limited utilization of electroactive sites can restrict its practical performance [2,6]. Incorporating MnO_2 into a conducting polymer matrix is one method to improving electrical transport and electrode performance [3,8-10].

Polyaniline (PANI)-MnO_2 nanocomposites have attracted interest due to the complementary properties of their constituent phases. PANI provides an electrically conducting and electrochemically active matrix, while MnO_2 contributes additional redox-active sites [10,11]. The resulting electrochemical performance depends on the composition, interfacial contact, particle distribution and morphology of the composite. The chemical oxidative polymerization, electrodeposition and interfacial polymerization have all been explored for preparing PANI-MnO_2 materials [11-14]. Interfacial polymerization is

This is an open access journal, and articles are distributed under the terms of the Attribution 4.0 International (CC BY 4.0) License. This license lets others distribute, remix, tweak, and build upon your work, even commercially, as long as they credit the author for the original creation. You must give appropriate credit, provide a link to the license, and indicate if changes were made.

particularly useful for controlling the reaction environment and polymer growth at an organic–aqueous boundary, which offer a route to composite structures with tailored morphologies [14,15].

In this study, a hierarchically structured PANI-MnO_2 nanocomposite was synthesized through static interfacial polymerization using $KMnO_4$ as both the oxidizing agent and the manganese precursor. The reaction was designed to enable PANI formation alongside the generation of the Mn-containing phase at the liquid-liquid interface. The resulting material exhibited a marigold-like architecture comprising mesopores and larger pore domains. Such a pore structure may improve electrolyte accessibility and facilitate ion transport within the electrode, although its contribution to charge-storage performance requires interpretation alongside the electrochemical results [12,14,15].

PANI-MnO_2 composites with a range of morphologies have been reported using different preparation routes including methods that incorporate preformed MnO_2 nanoparticles or separately synthesized manganese oxide structures into a polymer matrix [11-14]. The present method, in this work, differs in its use of $KMnO_4$ as both the oxidant for aniline polymerization and the source of the manganese containing phase. This strategy allows the formation of the polymer and inorganic component to occur within the same interfacial reaction system, potentially promoting close contact between the two phases. The focus of this work is to examine the relationship between the static interfacial synthesis route, the resulting hierarchical morphology and the electrochemical behaviour of the nanocomposite. The novelty claim is confined to this specific synthesis method and its structure performance relationship, rather than to the PANI-MnO_2 composition or hierarchical morphology themselves.

EXPERIMENTAL

Aniline, potassium permanganate, chloroform, perchloric acid, potassium hydroxide and N-methyl-2-pyrrolidone (NMP) were used in the synthesis and electrochemical evaluation of the PANI-MnO_2 nanocomposite. Poly(vinylidene fluoride) (PVDF) and acetylene black were used as the binder and conductive additive, respectively, during working-electrode preparation. All analytical reagents were of analytical-reagent (AR) grade and were used as received, without further purification.

Synthesis: The polyaniline-MnO_2 nanocomposite was synthesized *via* static interfacial polymerization. Based on the preliminary optimization experiments, an aniline/$KMnO_4$ molar ratio of approximately 4:1 was selected. Accordingly, 0.5 mL of aniline and 0.2 g of $KMnO_4$ were used. Aniline (0.5 mL) was dissolved in 50 mL of chloroform to prepare the organic phase, while $KMnO_4$ (0.2 g) was dissolved in 50 mL of 2 M perchloric acid to prepare the aqueous phase. The aqueous phase was carefully added to the organic phase, initiating polymerization at the liquid–liquid interface. The reaction was maintained for 24 h. The resulting material was washed repeatedly with distilled water until the filtrate became colourless and then dried in a vacuum oven before characterization and electrochemical testing.

Characterization: UV-Vis spectra of the PANI-MnO_2 nanocomposite were recorded using a Perkin-Elmer Lambda 25 double-beam spectrophotometer over the wavelength range of 300-900 nm. FT-IR spectra were acquired using a Bruker Tensor 37 ATR-FTIR spectrophotometer over the wavenumber range of 4000-400 cm^{-1}. Surface morphology was examined using a Hitachi S-4800 II field-emission scanning electron microscope (FE-SEM). X-ray diffraction (XRD) patterns were recorded using a Bruker D8 Advance diffractometer over a 2θ range of 10-90º with Cu*K*α radiation. The morphology and internal structure of the PANI-MnO_2 nanocomposite were examined using a JEOL JEM-2100 transmission electron microscope equipped with an energy-dispersive X-ray spectroscopy (EDX) detector, which was used to analyze its elemental composition.

Electrochemical performance evaluation: The electrochemical performance of pristine PANI and the PANI-MnO_2 nanocomposite was evaluated using cyclic voltammetry (CV), galvanostatic charge–discharge (GCD) and electrochemical impedance spectroscopy (EIS). CV measurements were used to examine the redox activity and charge-storage behaviour of the electrode materials [8]. The working electrode was prepared by mixing the active material (85 wt.%), poly(vinylidene fluoride) (PVDF, 5 wt.%) as a binder and acetylene black (10 wt.%) as a conductive additive in NMP to obtain a uniform slurry. Approximately 2 mg of slurry was deposited onto a clean glassy carbon electrode and dried in an oven at 80 ºC overnight. The electrochemical measurements were conducted in a conventional three-electrode cell containing 1 M KOH as the electrolyte. The prepared electrode served as the working electrode, a platinum electrode as the counter electrode and an Ag/AgCl electrode as the reference electrode.

RESULTS AND DISCUSSION

The formation of PANI-MnO_2 nanocomposites *via* interfacial polymerization is a redox reaction at the interface of a biphasic system immiscible with water and chloroform. In this process, the monomeric aniline from the organic phase was chemically oxidized by the MnO_4 ions present in the aqueous phase and is reduced to MnO_2. The formed MnO_2 was embedded in the polymer matrix, which results in the formation of PANI-MnO_2 nanocomposite. The formed nanocomposite was obtained in the hydrophilic emerald salt form, which diffused into the aqueous layer.

UV-Vis electronic absorption spectra: Fig. 1 shows the UV-Vis absorption spectrum of the PANI-MnO_2 nanocomposite. A sharp but low-intensity absorption band observed at approximately 340 nm was attributed to the presence of MnO_2 nanoparticles [16]. The characteristic absorption bands at approximately 470 and 800 nm correspond to π-polaron and polaron-π* electronic transitions, respectively, which confirm the formation of the doped state of polyaniline [8,11]. The observed polaron transitions are consistent with the doped state of PANI and the presence of delocalized charge carriers in the composite. The stronger absorption bands associated with PANI relative to those assigned to MnO_2 suggest that the spectral response is largely governed by the polyaniline component.

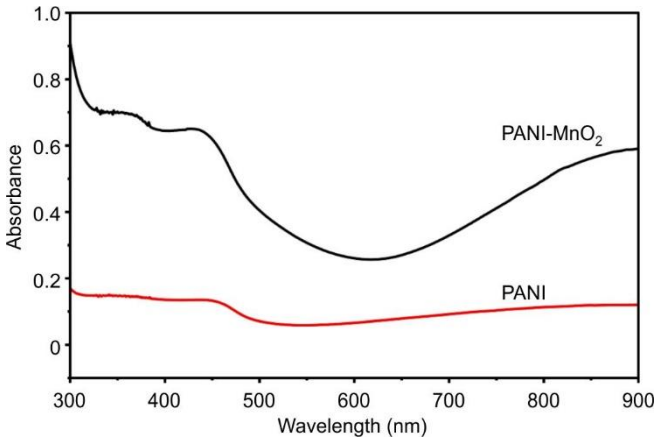


Fig. 1. UV-Vis spectra of pure PANI and PANI-MnO_2 nanocomposite

FT-IR spectra: The FT-IR spectra of pure polyaniline (PANI) and the PANI-MnO_2 nanocomposite are shown in Fig. 2. The FT-IR spectrum of PANI exhibits a broad absorption band near 3400 cm^{-1} attributed to N–H stretching vibrations and a band around 800 cm^{-1} associated with out-of-plane C–H bending of the aromatic rings. The bands within 1300-1000 cm^{-1} arise from C–N stretching and aromatic ring vibrations of the polymer backbone while the characteristic bands near 1560 and 1480 cm^{-1} correspond to quinoid and benzenoid ring stretching respectively and are consistent with the emeraldine form of PANI. The band around 1290 cm^{-1} is assigned to C–N stretching in secondary aromatic amines whereas the absorption near 1140 cm^{-1} is associated with vibrational modes linked to protonation and polaron formation in conductive PANI.

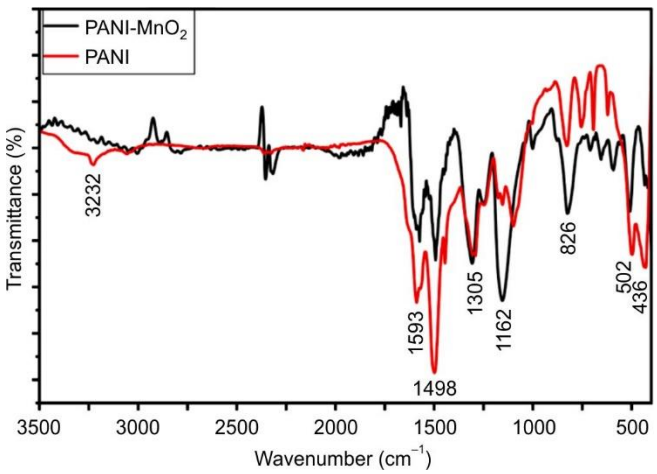


Fig. 2. FT-IR spectra of pure PANI and PANI–MnO_2 nanocomposite

Upon incorporation of MnO_2, the quinoid and benzenoid bands shift slightly towards lower wavenumbers and exhibit moderate broadening, which is consistent with changes in the chemical environment of the PANI chains following composite formation. The reduced intensity of the C–N stretching band may reflect interactions involving nitrogen containing groups at the PANI-MnO_2 interface. The appearance of additional bands near 620 520 and 480 cm^{-1} is attributed to Mn–O vibrations and supports the presence of MnO_2 in the composite. These spectral features support the incorporation of MnO_2 into the PANI matrix and are consistent with interfacial interactions between the two components.

X-ray diffraction (XRD): The XRD analysis was performed to examine the crystalline nature of the PANI-MnO_2 nanocomposite and the corresponding pattern is shown in Fig. 3. The presence of high-intensity diffraction peaks at 2θ = 19.25º and 25.79º indicates the dominance of polyaniline in the nanocomposite. The XRD pattern of MnO_2 exhibits broad diffraction peaks that are consistent with the presence of more than one structural phase. The reflections at 2θ values of 28.7º, 36.59º, 43.10º and 50.57º are assigned to γ-MnO_2 (JCPDS card no. 14-0644) [17] while those at 11.9º, 18.35º, 28.6º, 39.5º and 49.3º correspond to γ-MnO_2 (JCPDS card no. 44-0141) [6,17]. The coexistence of these diffraction features may be related to the interfacial reaction conditions under which PANI and the manganese oxide phase form. Several reflections of α-MnO_2 and γ-MnO_2 occur at similar 2θ positions and overlap within the broad diffraction profile which limits reliable estimation of their relative phase fractions by peak-intensity analysis. The XRD data are therefore interpreted as evidence of structural features associated with both phases rather than a quantitative determination of their proportions. The broad diffraction peaks are consistent with small crystallite dimensions and possible structural disorder in the composite. The average crystallite size was estimated to be approximately 30 nm using the Debye–Scherrer equation although this value remains approximate since peak broadening may arise from finite crystallite size as well as lattice strain instrumental effects and overlapping reflections.

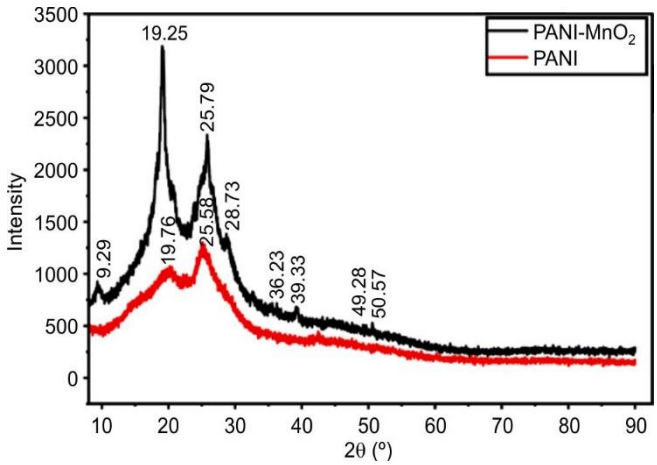


Fig. 3. XRD patterns of pure PANI and PANI-MnO_2

Thermal studies: Thermogravimetric analysis (TGA) was performed to investigate the thermal stability of the pristine polyaniline (PANI) and PANI-MnO_2 nanocomposite, as shown in Fig. 4. Both samples exhibited multistep decomposition behaviour. The initial weight loss of approximately 5% below 150 ºC is attributed to the removal of physically adsorbed moisture and surface-bound water molecules present in the polymer matrix and oxide component. The second stage of decomposition occurs between 150 and 400 ºC and is associated with the removal of dopant species and strongly retained water molecules from the polymer structure. Above 400 ºC the pronounced weight loss is attributed to the degra-

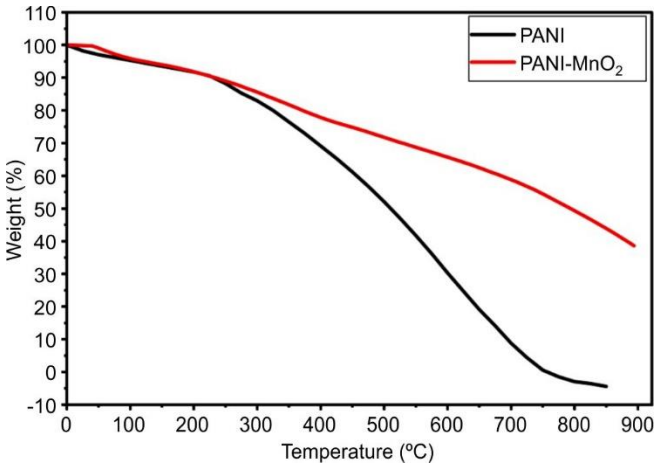


Fig. 4. Thermograms of pure PANI and PANI-MnO_2 nanocomposite

dation of the PANI backbone [14,15]. Pristine PANI undergoes rapid decomposition between 400 and 800 ºC with little residue remaining at the end of the heating cycle. The PANI-MnO_2 nanocomposite exhibits a lower weight loss and higher residual mass over the same temperature range. This behaviour points to improved thermal resistance following the incorporation of MnO_2. Interactions between the polymer chains and the MnO_2 surface may restrict chain mobility and slow the decomposition process. The higher residue at elevated temperatures is consistent with the presence of thermally stable MnO_2 in the composite.

Morphological studies: The morphology and microstructure of the polyaniline-MnO_2 nanocomposite are examined by FESEM and TEM, as shown in Figs. 5 and 6, respectively. The FESEM images (Fig. 5) show aggregates of approximately spherical, flower-like structures at lower magnification, while the higher-magnification images reveal a rough surface composed of interconnected irregular features. This morphology suggests the formation of a structured polymer–inorganic composite with an interconnected surface texture. The observed aggregation and surface roughness may influence the accessibility of the material surface, although specific surface area and pore-size distribution measurements are required to establish its porosity and textural properties.

TEM images (Fig. 6a-c) show aggregated structures with contrasting electron density, potentially arising from differences in composition and specimen thickness. The darker regions

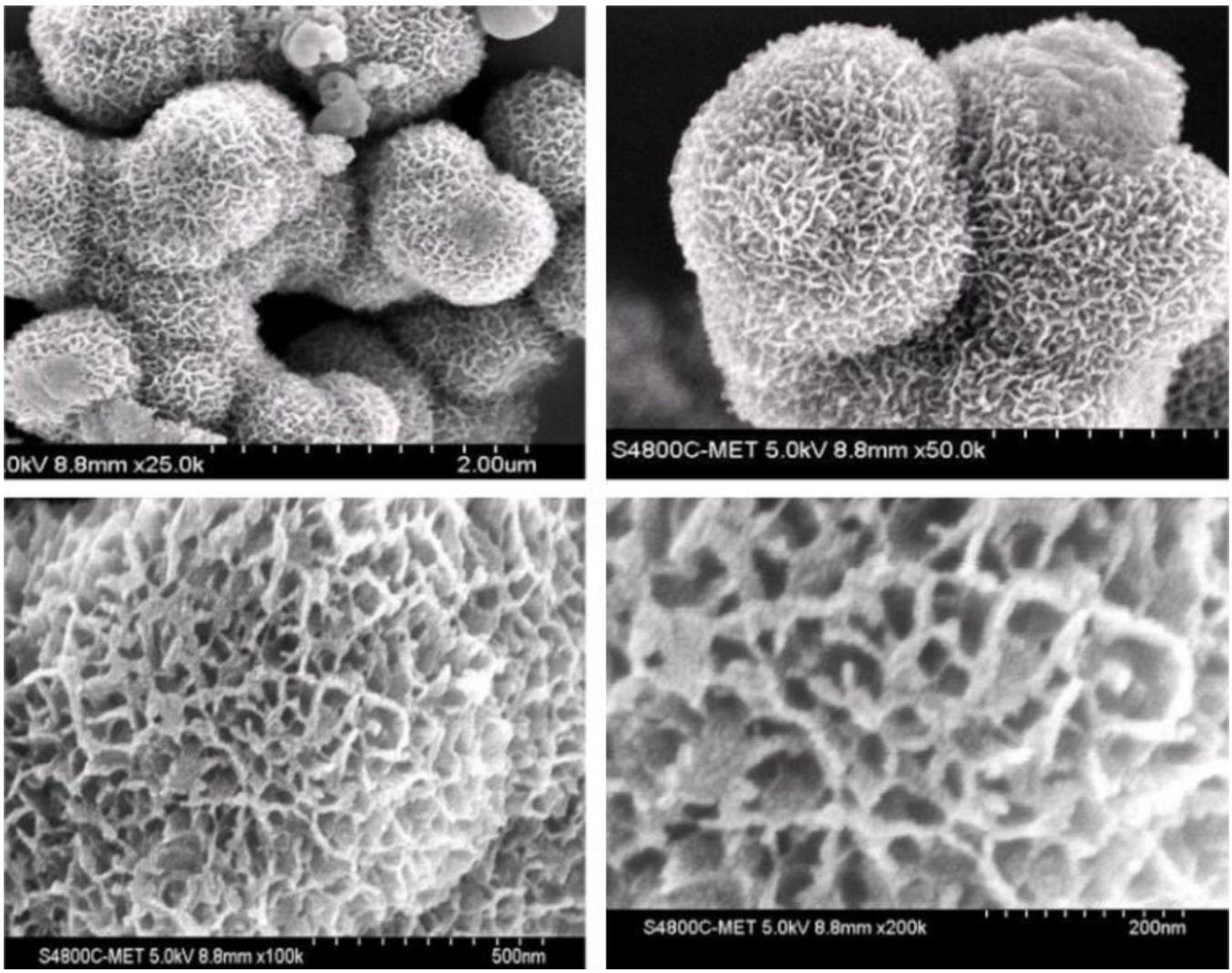


Fig. 5. FE-SEM images of polyaniline-MnO_2 nanocomposite

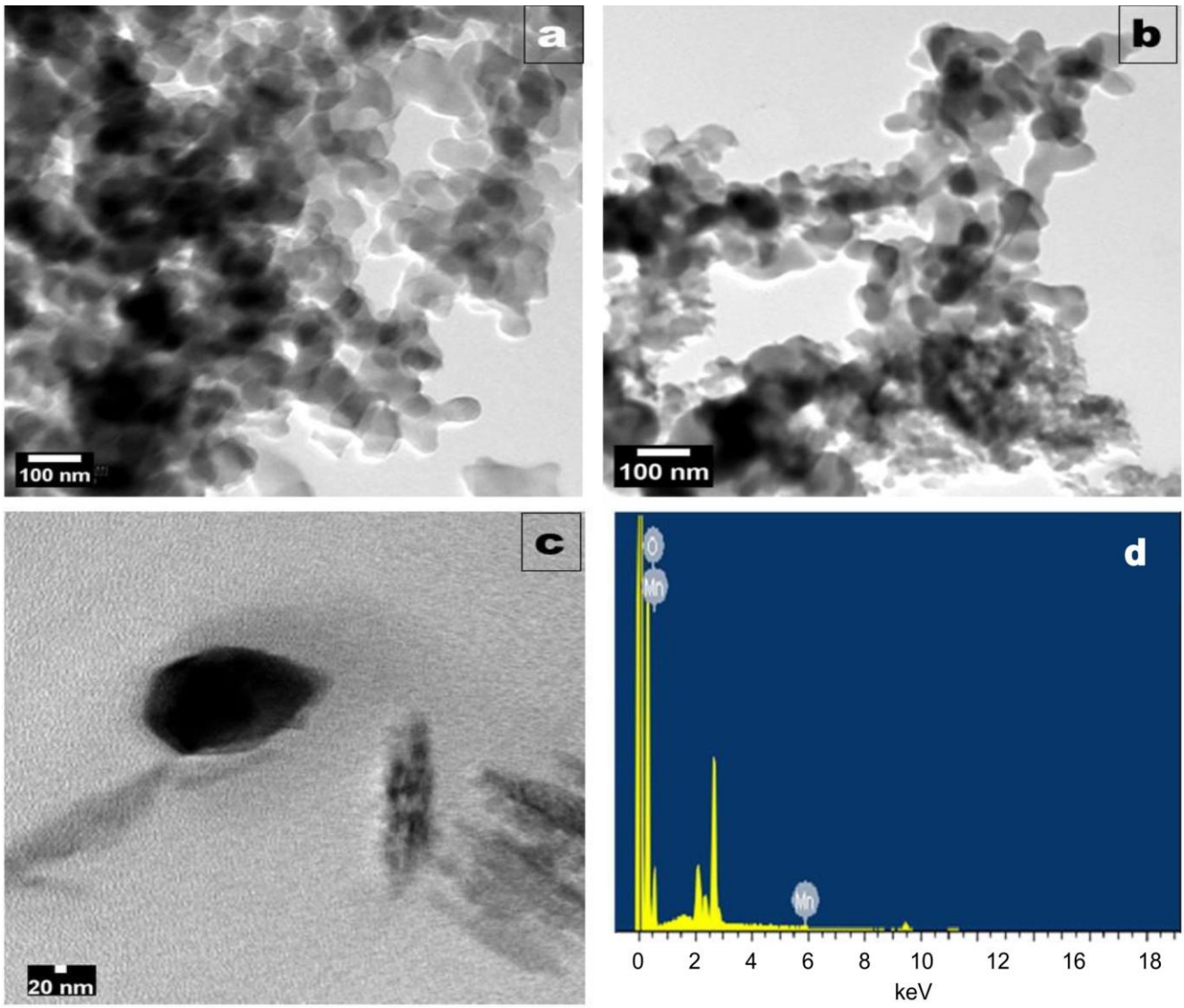


Fig. 6. TEM images and EDX spectrum of polyaniline-MnO_2 nanocomposite

may correspond to MnO_2-rich domains within the polyaniline matrix, although elemental mapping is required to confirm their distribution. The images do not provide sufficient evidence to establish a hollow structure or distinct nanofibre morphology. The EDX spectrum (Fig. 6d) confirms the presence of carbon, nitrogen, manganese and oxygen, consistent with the expected elemental composition of the composite.

BET analysis: Nitrogen adsorption–desorption measurements were performed to investigate the specific surface area and pore structure of the synthesized PANI-MnO_2 nanocomposite and the corresponding isotherm is shown in Fig. 7. The N_2 adsorption–desorption isotherm exhibited features associated with type II and type IV isotherms under the IUPAC classification which may reflect the presence of pores of different sizes within the nanocomposite [15]. The BET specific surface area was calculated to be 34.31 $m^2 g^{-1}$. The nitrogen uptake at low relative pressures ($P/P_o < 0.1$) was followed by a gradual increase across the intermediate pressure region consistent with surface adsorption and pore filling. The hysteresis loop at higher relative pressures suggests capillary condensation within the mesopores while its shape may be associated with slit-like voids formed by the assembled nanostructures. The sharp rise in nitrogen uptake near $P/P_o \approx 0.9$

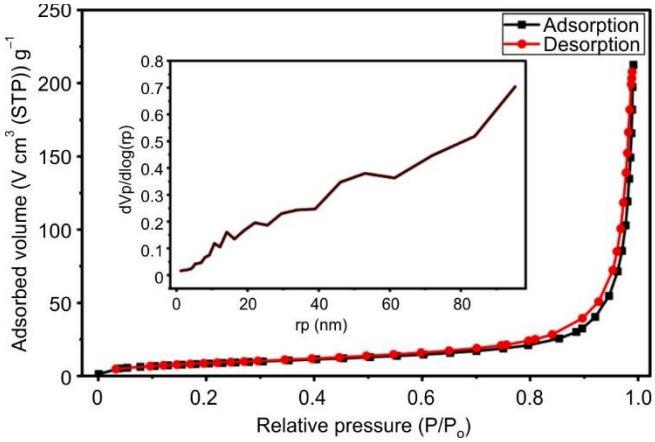


Fig. 7. N_2 adsorption-desorption isotherm with their respective pore size distribution for PANI-MnO_2 nanocomposite (inside graph)

points to additional condensation in larger pores or inter-particle voids. These textural features are consistent with the hierarchical architecture of the nanocomposite although confirmation of macroporosity requires pore-size analysis since nitrogen adsorption alone may not distinguish true macropores from voids between aggregated particles.

The Barrett–Joyner–Halenda (BJH) pore size distribution analysis revealed pore diameters predominantly in the range of 10-80 nm, which suggest the presence of mesopores and larger pores within the nanocomposite. These findings are consistent with the hierarchical marigold-like morphology observed in the SEM images. The interconnected porous structure may facilitate electrolyte penetration and ion transport by providing accessible pathways to electroactive sites. Along with the electrical conductivity of PANI and the redox activity of MnO_2, these textural features may contribute to the electrochemical performance of the PANI-MnO_2 nanocomposite.

Electrochemical studies: The electrochemical properties of pristine PANI and the synthesized PANI-MnO_2 nanocomposite were systematically investigated using cyclic voltammetry (CV), galvanostatic charge-discharge (GCD) and electrochemical impedance spectroscopy (EIS). The cyclic voltammetry (CV) measurements were performed in a three-electrode configuration using the prepared material as the working electrode, platinum as the counter electrode and Ag/AgCl as the reference electrode in a 1 M KOH electrolyte. Although polyaniline is known to undergo partial dedoping in alkaline electrolytes, the incorporation of MnO_2 improves the electrochemical activity and structural stability of the composite electrode through synergistic interfacial interactions. The CV measurements were performed at scan rates of 5-100 mV s^{-1} The CV curves of pristine PANI and the PANI-MnO_2 nanocomposite were obtained within the potential window of 0.2 to 0.75 V at scan rates of 5, 10, 20, 50 and 100 mV s^{-1}, as shown in Fig. 8.

The CV profiles exhibit broad anodic and cathodic redox peaks with non-rectangular characteristics, indicating hybrid battery-type/pseudocapacitive charge-storage behaviour arising from combined faradaic and non-faradaic processes [10,18]. Compared with pristine PANI, the PANI-MnO_2 nanocomposite exhibited a significantly larger enclosed CV area and higher current response at all scan rates indicate an enhanced electrochemical activity and improved charge storage capability after the incorporation of MnO_2 nanoparticles.

The electrochemical response of the PANI-MnO_2 nanocomposite arises from combined diffusion-assisted Faradaic reactions and surface-controlled charge storage processes, with a minor contribution from electric double-layer capacitance. The observed redox peaks were attributed to the reversible transition between the leucoemeraldine and emeraldine salt forms of polyaniline along with the Mn^{4+}/Mn^{3+} redox transitions of MnO_2 [10,18]. The enhanced electrochemical performance may be attributed to the synergistic interaction between conductive PANI and electroactive MnO_2, which facilitates electron transport and provides abundant redox-active sites for charge storage in the material.

The specific capacitance values calculated from the CV curves were 751, 539, 282, 184 and 142 F g^{-1} at scan rates of 5, 10, 20, 50 and 100 mV s^{-1}, respectively, which are higher than those obtained for pristine PANI and several previously reported PANI/MnO_2-based electrodes [11,18]. The gradual decrease in the specific capacitance with increasing scan rate is attributed to the insufficient diffusion of electrolyte ions into the inner electroactive sites of the electrode material at higher polarization rates. Since, the CV and GCD profiles indicated non-ideal capacitive behaviour with a significant Faradaic contribution, the electrochemical performance was further evaluated using the GCD-derived capacitance values. To further elucidate the electrochemical kinetics of the electrodes, the relationship between the peak current and scan rate was analyzed according to the power-law equation:

$$i = av^b$$

where i represents the peak current; v is the scan rate and a and b are the adjustable parameters. The calculated b-values for pristine PANI and the PANI-MnO_2 nanocomposite were 0.41 and 0.62, respectively. The lower b-value of pristine PANI indicates predominantly diffusion controlled charge storage behaviour, whereas the increased b-value of the composite suggests an enhanced surface-controlled pseudocapacitive contribution and improved charge-transfer kinetics arising from the synergistic interaction between PANI and MnO_2. Furthermore, the intermediate b-value obtained for the comp-

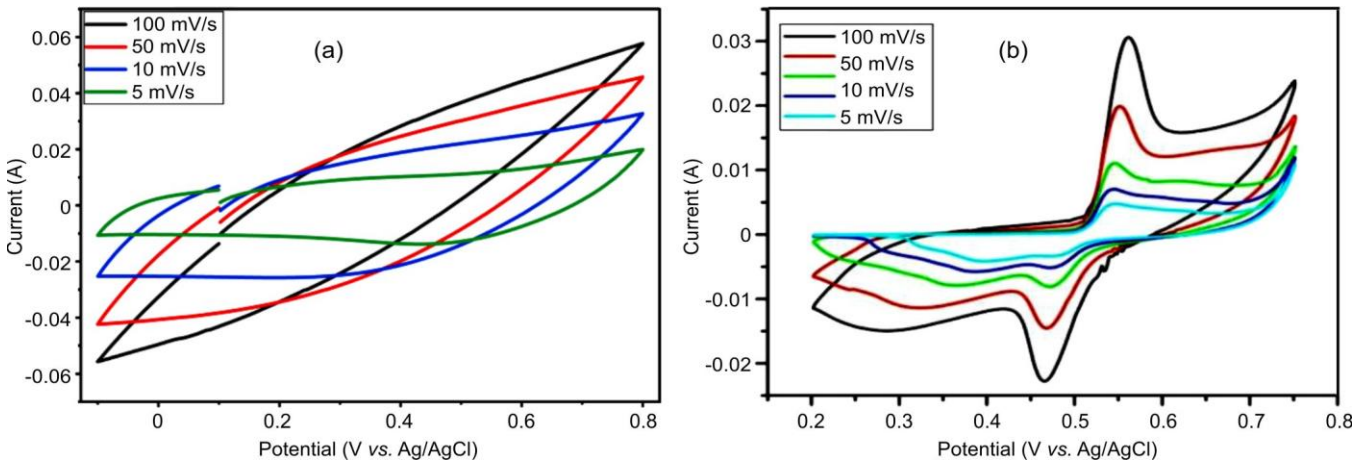


Fig. 8. Cyclic voltammograms of (a) pure PANI and (b) PANI-MnO_2 nanocomposite at different scan rates

osite confirms the coexistence of diffusion-assisted Faradaic reactions and capacitive charge storage processes within the electrode material, which is consistent with the redox features observed in the CV curves.

The Galvanostatic charge–discharge measurements were performed at current densities ranging from 0.5 to 10 A g^{-1} (Fig. 9a-b). The GCD curves exhibited nonlinear profiles with distinct voltage plateaus, which suggest that reversible faradaic redox reactions contribute to the charge-storage mechanism. The observable IR drop reflects the internal resistance of the electrode system and may arise from ohmic resistance and interfacial charge-transfer limitations. The reasonably symmetric charge–discharge profiles indicate favourable electrochemical reversibility under the tested conditions [1,3]. The specific capacitance values were calculated using:

$$Csp = \frac{I\Delta t}{m\Delta V}$$

where ΔV represents the potential window excluding the IR drop, were 483, 468, 435, 311 and 223 F g^{-1} at current densities of 0.5, 1, 2, 5 and 10 A g^{-1}, respectively. The reduction in capacitance at higher current densities is attributed to restricted ion diffusion and incomplete utilization of electroactive sites during rapid charge–discharge processes [9]. Long-term cycling stability evaluated over 2500 cycles at 0.5 A g^{-1} showed capacitance retention of approximately 91% confirm the good electrochemical durability of the nanocomposite electrode [18]. The improved electrochemical performance was related with the hierarchical marigold-like mesoporous architecture of the composite. The interconnected porous framework facilitates rapid electrolyte penetration and ion diffusion, while the hollow domains provide additional electroactive sites and buffering space for reversible redox reactions [19].

Electrochemical impedance spectroscopy was employed to investigate the charge-transfer characteristics. The Nyquist plot (Fig. 10) exhibits a small semi-circle in the high frequency region corresponding to the charge-transfer resistance, followed by an inclined line in the low-frequency region associated with the pseudocapacitive behaviour and diffusion assisted ion transport [8]. The deviation from a perfectly vertical

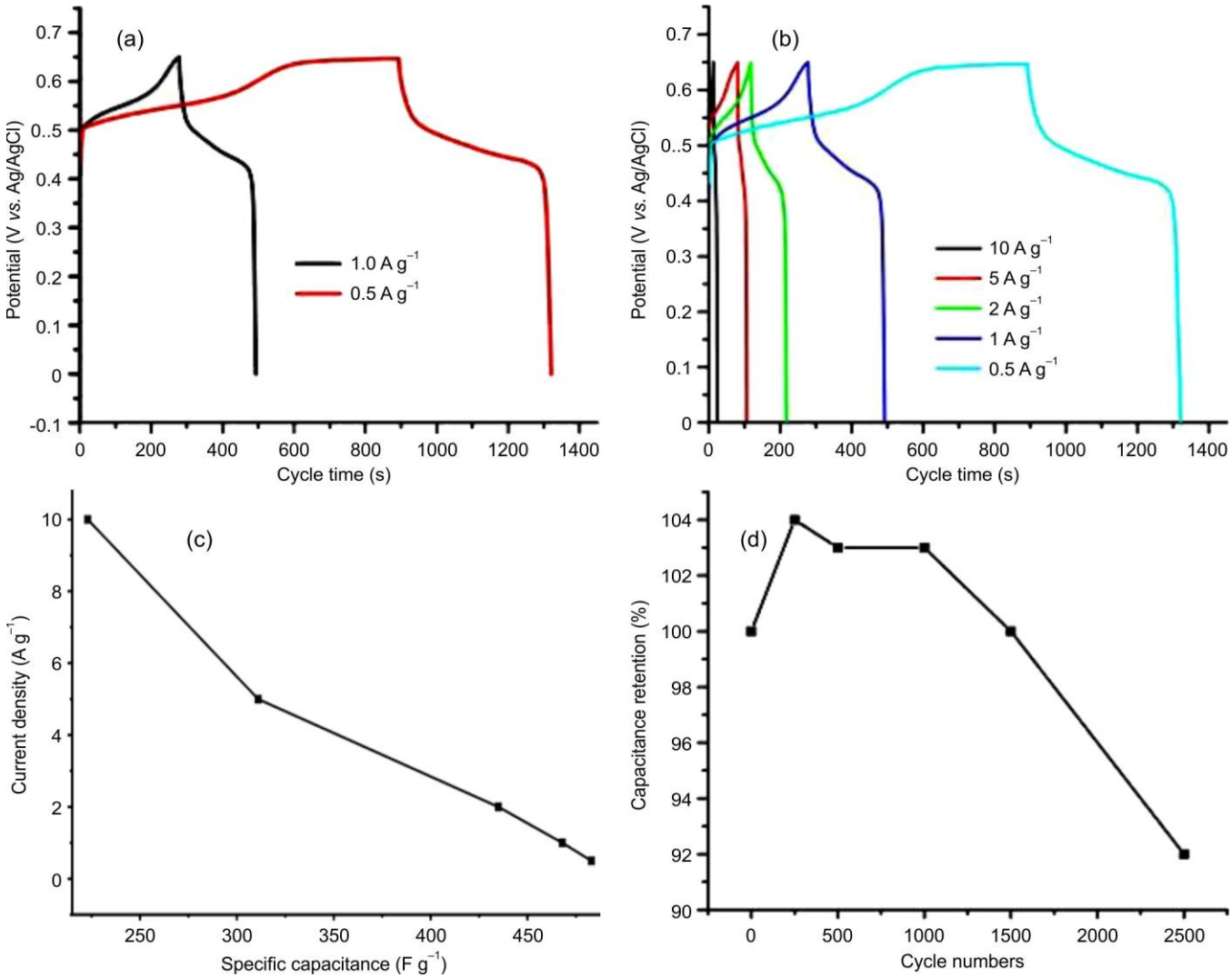


Fig. 9. (a) Galvanostatic charge-discharge curves at 0.5 and 1 A g^{-1}, (b) galvanostatic charge-discharge curves at various current densities, (c) dependence of specific capacitance on the current density, and (d) capacitance retention of the electrode material over 2500 charge–discharge cycles

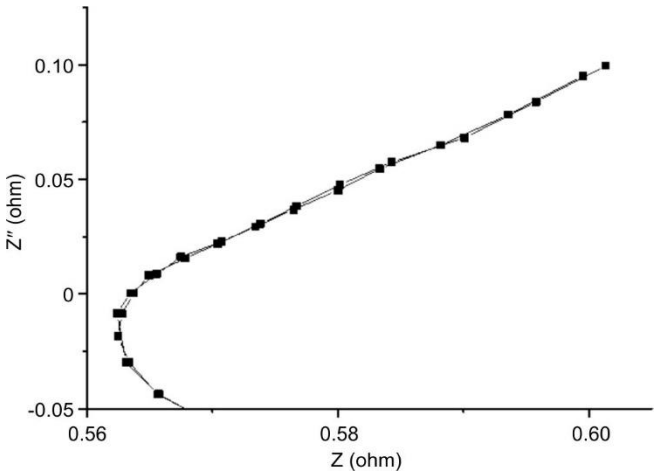


Fig. 10. Nyquist plot of PANI-MnO_2 nanocomposite

line indicates the presence of Faradaic and diffusion controlled processes within the electrode. The low charge-transfer resistance obtained from the impedance spectrum (~0.56 Ω) suggests efficient electron transport and favourable electrochemical kinetics owing to the strong interfacial interaction between PANI and MnO_2 [18,20]. The combined CV, GCD, b-value and EIS analyses suggest that the PANI-MnO_2 nanocomposite exhibits hybrid pseudocapacitive behaviour involving both diffusion-controlled Faradaic reactions and surface controlled charge-storage processes.

Conclusion

The PANI-MnO_2 nanocomposite was successfully synthesized through static interfacial polymerization and characterized using spectroscopic, structural, morphological and electrochemical techniques. The characterization results supported the incorporation of MnO_2 into the PANI matrix and revealed a hierarchical marigold like architecture with a BET surface area of 34.31 $m^2 g^{-1}$. This porous structure may facilitate electrolyte penetration and improve access to electroactive sites. The electrochemical measurements revealed enhanced charge-storage performance compared with pristine PANI. The composite exhibited a CV-derived specific capacitance of 751 F g^{-1} at 5 mV s^{-1} and a GCD-derived value of 483 F g^{-1} at 0.5 A g^{-1}. It retained approximately 91% of its initial capacitance after 2500 charge–discharge cycles and exhibited a charge-transfer resistance of about 0.56 Ω. The intermediate b-value of 0.62 further supported the contribution of both diffusion controlled Faradaic reactions and surface-controlled charge-storage processes. These findings suggest that combining PANI with MnO_2 can improve the electrochemical response and cycling stability of the electrode. The results establish the PANI-MnO_2 composite as a promising candidate for supercapacitor electrodes, although further studies involving longer cycling tests, reproducibility assessments and evaluation under practical device conditions are required to establish its suitability for energy-storage applications.

ACKNOWLEDGEMENTS

One of the authors, MK thanks the Ministry of Electronics and Information Technology, Government of India and Director, C-MET, Pune, for providing the instrumentation facilities.

CONFLICT OF INTEREST

The authors declare that there is no conflicts of interest regarding the publication of this article.

DECLARATION OF AI-ASSISTED TECHNOLOGIES

During the preparation of this manuscript, the authors used an AI-assisted tool(s) to improve the language and no data, results or scientific conclusions were generated by AI. All analyses, interpretations and conclusions are the authors' own. The authors reviewed and edited the content and take full responsibility for the published work.

REFERENCES

1. I.O. Oladele, S.O. Adelani, A.S. Taiwo, I.M. Akinbamiyorin and O.F. Olanrewaju, *RSC Adv.*, **15**, 7509 (2025); https://doi.org/10.1039/D4RA08601E
2. M. Shah, D. West and V. Balakotaiah, *Chem. Eng. J.*, **452**, 139365 (2023); https://doi.org/10.1016/j.cej.2022.139365
3. A. Tundwal, H. Kumar, B.J. Binoj, R. Sharma, G. Kumar, R. Kumari, A. Dhayal, A. Yadav, D. Singh and P. Kumar, *RSC Adv.*, **14**, 9406 (2024); https://doi.org/10.1039/D3RA08312H
4. M.F. Ahmer, Q. Ullah and M.K. Uddin, *J. Polym. Eng.*, **45**, 1 (2025); https://doi.org/10.1515/polyeng-2024-0101
5. S.M. Alsufyani, R. Jafer, J. Iqbal, R. Alwafi, S. Bashir, S. Ramesh and K. Ramesh, *J. Energy Storage*, **84**, 110713 (2024); https://doi.org/10.1016/j.est.2024.110713
6. R. Liang, Y. Du, P. Xiao, J. Cheng, S. Yuan, Y. Chen, J. Yuan and J. Chen, *Nanomaterials*, **11**, 1248 (2021); https://doi.org/10.3390/nano11051248
7. L. Plakia and I.A. Kartsonakis, *Energies*, **18**, 3455 (2025); https://doi.org/10.3390/en18133455
8. X. Song, H. Wang, Z. Li, C.-F. Du and R. Guo, *Chem. Rec.*, **22**, e202200118 (2022); https://doi.org/10.1002/tcr.202200118
9. W. Ni, D. Wang, Z. Huang, J. Zhao and G. Cui, *Mater. Chem. Phys.*, **124**, 1151 (2010); https://doi.org/10.1016/j.matchemphys.2010.08.050
10. A.H. Gemeay, R.G. El-Sharkawy, I.A. Mansour and A.B. Zaki, *J. Colloid Interface Sci.*, **308**, 385 (2007); https://doi.org/10.1016/j.jcis.2006.12.077
11. Jaidev, R.I. Jafri, A.K. Mishra and S. Ramaprabhu, *J. Mater. Chem.*, **21**, 17601 (2011); https://doi.org/10.1039/c1jm13191e
12. S. Chen, Y. Zhang, D. Tian, Q. You, M. Zhong, C. Hu and J. Chen, *Electrochim. Acta*, **450**, 142275 (2023); https://doi.org/10.1016/j.electacta.2023.142275
13. R.H. Patil, V.V. Kulkarni, T.D. Dongale and S.A. Jadhav, *J. Compos. Sci.*, **7**, 167 (2023); https://doi.org/10.3390/jcs7040167
14. J.G. Wang, Y. Yang, Z.H. Huang and F. Kang, *J. Power Sources*, **204**, 236 (2012); https://doi.org/10.1016/j.jpowsour.2011.12.057
15. F. Hoffmann, M. Cornelius, J. Morell and M. Fröba, *Angew. Chem. Int. Ed.*, **45**, 3216 (2006); https://doi.org/10.1002/anie.200503075
16. A.N. Naveen and S. Selladurai, *Electrochim. Acta*, **125**, 404 (2014); https://doi.org/10.1016/j.electacta.2014.01.161
17. L. Li, Y. Pan, L. Chen and G. Li, *J. Solid State Chem.*, **180**, 2896 (2007); https://doi.org/10.1016/j.jssc.2007.08.017
18. R. Devi, V. Kumar, S. Kumar, M. Bulla, S. Sharma and A. Sharma, *Appl. Sci.*, **13**, 7907 (2023); https://doi.org/10.3390/app13137907
19. B.E. Conway, Electrochemical Supercapacitors: Scientific Fundamentals and Technological Applications, Kluwer Academic/Plenum Publishers, New York (1999); https://doi.org/10.1007/978-1-4757-3058-6
20. S. Vijayakumar, S. Nagamuthu and G. Muralidharan, *ACS Appl. Mater. Interfaces*, **5**, 2188 (2013); https://doi.org/10.1021/am400012h